

A Numerical Investigation of Stresses, Printing Efficiency, Printability, and Cell Viability in Nozzle Printheads for 3D Extrusion Bioprinting

Okano Lab. ZHANG, Colin

Introduction

3D (three-dimensional) extrusion bioprinting is a rapidly developing field in tissue engineering. Recent advances have ushered in a new stage of producing customized and bioengineered structures in regenerative medicine, pharmacokinetics, and basic cell biology studies. 3D extrusion bioprinters are the most widely used devices for various types of bioprinting devices because of their good cost-effectiveness and simple operation.¹ They extrude bioinks (hydrogels that contain living cells) from needles to form filaments and scaffolds that can later be cross-linked and used to construct desired biostructures.

During the extrusion, controlling stresses inside the needle is a major factor in balancing printing resolution and cell viability.² As experimentally observing stresses inside the needle is complex, and testing thousands of bioink with different kinds of rheological properties is a tedious and repetitive process, the need to utilize numerical simulation to understand and optimize needle geometries, printing efficiency, printability, and cell viability becomes an urgent task for 3D extrusion bioprinting devices.³ This research considers alginate-based bioinks since they are the most commonly used commercial bioinks due to low cost, biocompatibility, and facile gelation.⁴ Nonetheless, the numerical model can be easily modified to adapt various kinds of bioinks.

Numerical Method

The numerical simulation was carried out by OpenFOAM. The following assumptions are made when concerning the analytical solution and simulation: (I) the bioink acts as an incompressible power-law fluid (Ostwald–de Waele relationship) in which the shear stress, $\tau = K\dot{\gamma}^n$, and the apparent viscosity, $\eta = K\dot{\gamma}^{n-1}$, where K is the consistency index, n is the flow index (dimensionless), and $\dot{\gamma}$ is the shear rate. The non-Newtonian shear-thinning behavior of the bioink leads to $0 < n < 1$; (II) there is no slip between the bioink and the smooth needle wall; (III) the gravity influence is negligible due to the fine needle size; (IV) the flow inside the needle is fully developed and laminar.

The simulation was first validated against an analytical solution; the validation showed good alignments in both velocity profile and wall shear stress for a cylindrical needle with a radius, R , of $400 \mu\text{m}$, and a needle length, L_n , of 13 mm. The volumetric flow rate, Q , is set to $50 \mu\text{L}/\text{s}$; the 2.5% alginate (w/v) at 25°C has the following rheological properties: $K = 29.86 \text{ Pa}\cdot\text{s}^n$ and $n = 0.46$. The simulation was then carried out in the same fashion.

In addition to the needle region, the syringe head region was added to the numerical simulation to take into account the extensional stress near the inlet of the needle region, as shown in Fig. 1. The following governing equations were implemented in the numerical simulation:

- incompressible continuity equation,

$$\nabla \cdot \mathbf{U} = 0; \quad (1)$$

- steady-state Navier–Stokes equations,

$$\mathbf{U} \cdot \nabla \mathbf{U} - \nabla \cdot \left(\frac{\eta}{\rho} \nabla \mathbf{U} \right) = -\frac{\nabla P}{\rho}; \quad (2)$$

- Poisson equation for pressure,

$$\frac{\nabla^2 P}{\rho} = \nabla \cdot \left(\frac{\eta}{\rho} \nabla^2 \mathbf{U} - \mathbf{U} \cdot \nabla \mathbf{U} \right); \quad (3)$$

- shear rate (scalar),

$$\dot{\gamma} = \sqrt{\frac{1}{2} \nabla \mathbf{U} : \nabla \mathbf{U}}; \quad (4)$$

here, \mathbf{U} is the velocity vector, ρ is the density, and P is the pressure. The symbol “ $:$ ” represents the inner product of the two tensors. Finally, the apparent viscosity is calculated by the power law with a limiter on the maximum and minimum apparent viscosities to avoid divergence. Limiter values are chosen such that the apparent viscosity range in the simulation does not violate the experimental results in which the shear rate, $0.1 \leq \dot{\gamma} \leq 1000 \text{ s}^{-1}$.

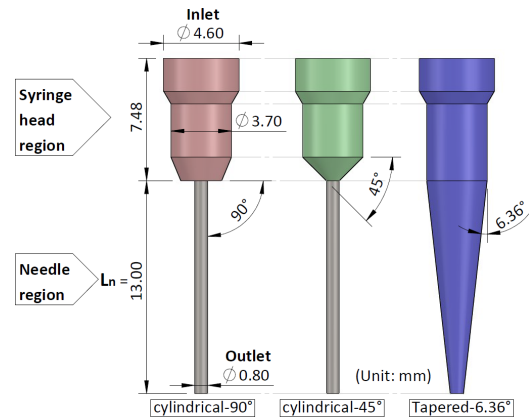


Figure 1: Dimensions of needles in the simulation.

Results & Discussion

This investigation numerically investigates three types of needles: 90° cylindrical needle, 45° cylindrical needle and tapered 6.36° needle (Fig. 1). Influences of needle geometries and temperature changes on the magnitudes of stresses are considered.

Needle types and assessment of stresses

Fig. 2 shows the simulation results of the stress distribution near the needle inlet/outlet region. The results demonstrate that the highest stress is caused by the extensional stress near the inlet region for cylindrical needles and the outlet for the tapered needle.

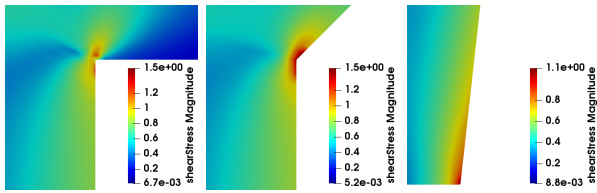


Figure 2: Stresses inside different types of needles.

Temperature influences on stresses

Sarker and Chen (2017) experimentally evaluated the temperature dependence of the 2.5% alginate (w/v) bioink's K and n values, shown in Table 1.⁵ If the volumetric flow rate, Q , is kept constant, a significant stress reduction is expected according to the power law, $\tau = K\dot{\gamma}^n$.

Temperature (°C)	25	35	45	55
K (Pa·s ⁿ)	29.86	18.50	12.53	5.13
n (-)	0.46	0.51	0.56	0.64

Table 1: The temperature dependency of K and n .

Since the cylindrical needle inlet region and the tapered needle outlet region exhibit the most significant stresses (both shear stress and extension stress), the stresses in these regions are investigated. The relationship between temperature change and stresses around the needle inlet/outlet region is depicted in Fig. 3. The arc length is the circumference cut by the sphere (bottom right of Fig. 3).

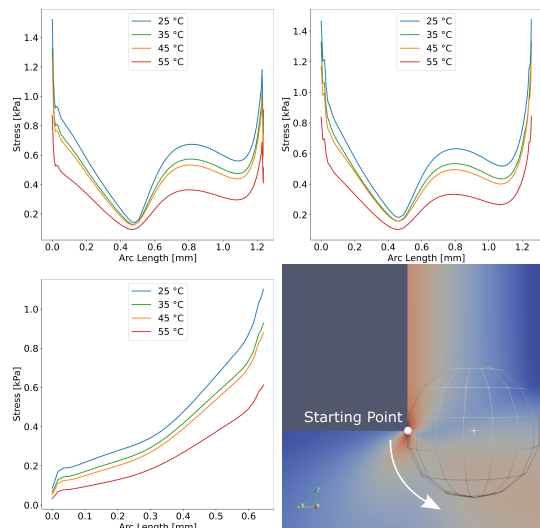


Figure 3: Top left: 90° cylindrical needle; top right: 45° cylindrical needle; bottom left: tapered needle; bottom right: arc length definition (rotating counter-clockwise).

Conclusion

Significant differences in shear stresses between cylindrical and tapered needles are observed when the volumetric flow rate, Q , is constant. Temperature change is also an essential factor in the magnitudes of stresses in both needles.

The 90° cylindrical needle has the highest maximum stress (1.53 kPa), but the area of such stress is much smaller (about 90% lower) when compared to its 45° counterpart (maximum stress is 1.48 kPa). The 90° cylindrical needle also has slightly higher stress (about 75 Pa) around the inlet region than the 45° counterpart.

The tapered needle has a minor stress in magnitude (1.10 kPa) and area. It does not have continuous and constant shear stress throughout the needle region, like cylindrical needles; significant extensional stress is only observed in the needle outlet region. The tapered needle can significantly increase cell viability due to low stresses and affected areas; however, when printing in a support bath, tapered needles can cause disturbance and should be avoided.

The temperature change significantly reduces the extensional stresses near the needle inlets for cylindrical needles. The relatively insignificant change in stresses when transitioning from 35°C to 45°C indicates a nonlinear relationship between temperatures and stresses. Furthermore, the low-stress regions do not have the same responses as the high-stress regions; the high-stress responses are much more aggressive (Fig. 3).

Future works

This research aims to understand and optimize needle geometries or the rheological properties of bioink during the printing process to increase cell viability. It is important to:

- ▶ investigate the gelation of bioinks and printed strands at various printing/extrusion speeds;
- ▶ determine how the concentration of alginate-based bioinks affects the stresses;
- ▶ optimize the printing/extrusion speed, environmental temperature, and cell viability for various types of bioinks and needle geometries;
- ▶ utilize machine learning to experimentally predict the cell viability with various parameters of needles and bioinks.

¹Y. S. Zhang et al., *Nature Reviews Methods Primers*, **1**(1), pp. 1–20, 2021

²Blaeser et al., *Advanced Healthcare Materials*, **5**(3), pp. 326–333, 2016

³H. Zhang et al., *Advanced Functional Materials*, **30**(13), p. 1910573, 2020

⁴Piras and Smith, *Journal of Materials Chemistry B*, **8**(36), pp. 8171–8188, 2020

⁵Sarker and Chen, *Journal of Manufacturing Science and Engineering*, **139**(8), p. 081002, 2017